Localized compliance measurement of the airway wall using anatomic optical coherence elastography

RUOFEI BU,[1] SANTOSH BALAKRISHNAN,[1] HILLEL PRICE,[2] CARLTON ZDANSKI,[3] SORIN MITRAN,[4] AND AMY L. OLDENBURG[1,2,5,*]

[1]*Department of Biomedical Engineering, University of North Carolina at Chapel Hill, Chapel Hill, NC 27599-3216, USA*

[2]*Department of Physics and Astronomy, University of North Carolina at Chapel Hill, Chapel Hill, NC 27599-3255, USA*

[3]*Department of Otolaryngology/Head and Neck Surgery, University of North Carolina at Chapel Hill, Chapel Hill, NC 27599-3255, USA*

[4]*Department of Mathematics, University of North Carolina at Chapel Hill, Chapel Hill, NC 27599-7070, USA*

[5]*Biomedical Research Imaging Center, University of North Carolina at Chapel Hill, Chapel Hill, NC 27599-7248, USA*

*aold@physics.unc.edu

Abstract: We describe an elastographic method to circumferentially-resolve airway wall compliance using endoscopic, anatomic optical coherence tomography (aOCT) combined with an intraluminal pressure catheter. The method was first demonstrated on notched silicone phantoms of known elastic modulus under respiratory ventilation, where localized compliance measurements were validated against those predicted by finite element modeling. Then, *ex vivo* porcine tracheas were scanned, and the pattern of compliance was found to be consistent with histological identification of the locations of (stiff) cartilage and (soft) muscle. This quantitative method may aid in diagnosis and monitoring of collapsible airway wall tissues in obstructive respiratory disorders.

1. Introduction

Biomedical elastography spatially-resolves the mechanical properties of tissue, which aids in diagnosis and monitoring of a variety of pathological conditions [1]. In airways, changes in luminal air pressure during normal (or ventilated) respiration drive deformation of the airway wall. The compliance of the airway wall (*i.e.*, the amount deformation per unit pressure) is dictated by the spatial pattern of airway wall elastic modulus, thickness, and smooth muscle activity. Quantitative measurements of compliance pinpoint tissues with high collapsibility that directly impact airflow; at the same time, longitudinal changes in, or mechanical modeling of compliance measurements can be used to elucidate temporal or spatial changes, respectively, in the underlying mechanical properties of the airway walls. As such, elastography has been used in the upper airways to study diseases like obstructive sleep apnea (OSA) [2,3]. Elastography can also elucidate the heterogeneous structure and behavior of the central airways [4], as relevant to disorders such as tracheomalacia that impair respiratory quality of life and can lead to rapidly fatal respiratory distress [5,6]. Overall, elastography could be very helpful in understanding the mechanisms of upper and central airway disorders and aid in diagnosis and monitoring of conditions associated with dynamic airway collapse. To this end, here we propose an endoscopic anatomic optical coherence tomography (aOCT) system for airway wall elastography. The system is demonstrated in excised tracheas from the central airways of pigs, with biomechanical properties mainly determined by tracheal cartilage and trachealis muscle, whose elastic moduli are several orders of magnitude

different [7]. The methods developed here may be broadly applicable to the study of upper and central airway disorders.

To date, several biomedical imaging modalities have been used for elastography of airway walls, such as magnetic resonance imaging (MRI) and ultrasound (US). Magnetic resonance elastography (MRE) has been used to assess elastic properties to characterize airway diseases such as OSA and obstructive lung disease [8,9]. However, MRE frequently requires sedation and cannot be performed on patients with MRI contraindications [10]. Compared to MRE, ultrasound has not been widely employed for airway elastography due to logistics of direct tissue contact. Exceptions like endobronchial ultrasound elastography are emerging [11], but have been primarily developed for detecting cancer infiltration in lymph nodes [12]. The limited speed, resolution, and deployment of these biomedical imaging modalities make airway wall elastography challenging. In contrast, aOCT provides high-speed, high resolution airway imaging that is favorable for capturing airway wall deformations during respiration that are small and rapid, and aOCT can be employed endoscopically during standard interventions [13].

The concept of performing elastography on an OCT platform, known as optical coherence elastography (OCE), was introduced in 1998 [14]. Since then, many studies related to OCE have been published, such as using phase-resolved OCT signals to produce a strain map with high displacement sensitivity [15,16], and using swept-source OCT (SSOCT) for endoscopic OCE [17,18]. For airway imaging, systems providing a larger imaging range and endoscopic capability to capture the airway lumen are desired. To address this need, aOCT, also known as long-range OCT, was developed to provide >10 mm imaging depth and coupled with an endoscopic, fiber-optic probe [19,20]. More recently, swept-source aOCT systems have been applied to study subglottic stenosis [21], inhalation injury [22] and asthma [23]. Considering the different means of excitation, OCE is categorized into two types: elastography achieved by measuring micron-level displacements under static compression, and by tracing the propagation of wave forms inside tissues under dynamic stimuli [24]. To quantify airway wall biomechanical properties, static elastography was performed using aOCT scans to capture lumen deformation combined with pressure measurement; this has been used to study mechanisms of obstructive airway disorders and dynamic airway collapse [19,25]. In these studies, airway compliance was treated as a global parameter within a given airway cross-section (*i.e.*, a cross-sectional compliance) which does not capture circumferential heterogeneity. A prior study that assessed a circumferentially-resolved radial strain in rabbit tracheas demonstrated a promising correlation between strain and underlying tissue constituents (trachealis muscle vs. cartilage) [17]. However, the ability to make such correlations can be confounded by mechanical coupling of regions with widely different elastic moduli, which can result in a non-intuitive pattern of deformation compared to the underlying pattern of biomechanical tissue properties. Also, measurements of pressure can be inaccurate when they are performed externally and not at the direct intraluminal site of deformation [26].

To address these limitations, this paper employs finite-element modeling (FEM) of simplified airway models to provide intuition about the pattern of deformation expected from a trachea-like phantom. At the same time, an intraluminal pressure catheter is employed simultaneously with the aOCT probe to ensure accuracy of ventilated respiratory pressures. We also propose a new method using the dynamic centroid of the lumen for computing a local (circumferentially-resolved) compliance, *LC*, which enhances the robustness of measurements to motion artifacts. The structure of the paper is as follows. Initially, aOCT scans of a uniform tube of known thickness and elastic modulus under dynamic respiratory ventilation was performed, and the experimentally-derived *LC* was compared to that from the thick-walled tube model to validate the magnitude of measured *LC*. Then, aOCT-derived patterns of *LC* were measured from a notched tube and compared to a finite element model of the tube for validation. The notched tube *LC* patterns also provided a qualitative interpretation

of the expected pattern of *LC* from porcine tracheas based upon their tissue heterogeneity. Finally, aOCT-derived patterns of *LC* were collected from *ex vivo* porcine tracheas to demonstrate how *LC* reveals the heterogeneity of airways caused by cartilage and trachealis muscle. This work demonstrates the ability of elastography measurements to reveal the heterogeneity of the airway circumferentially, as well as providing insight via FEM that explains the pattern of *LC* arising from heterogeneous elastic cylinders. Ultimately, we expect that this method could be extended to detect pathological tissues *in vivo* in human airways based on the pattern of *LC* measured during respiration.

2. Methods

2.1 Local compliance computation

In practice, compliance can be defined as a cross-sectional compliance [27] or as a diameter compliance [28]. To capture the heterogeneous nature of the airway wall, we define a circumferentially-resolved compliance (called local compliance, $LC(\theta)$), which is similar to a diameter compliance. The local compliance is subsequently computed as the change of lumen radius over change in intraluminal pressure at each polar angle according to:

$$LC(\theta) = \frac{\Delta u_\theta}{\Delta p} = \frac{u_{\theta, p_{max}} - u_{\theta, p_{min}}}{p_{max} - p_{min}} \tag{1}$$

in which u_θ is the radius at polar angle θ, and p is intraluminal pressure; the radial displacement Δu_θ is defined as the difference between radii when pressure is at its maximum p_{max} and minimum p_{min}, as shown in Fig. 1.
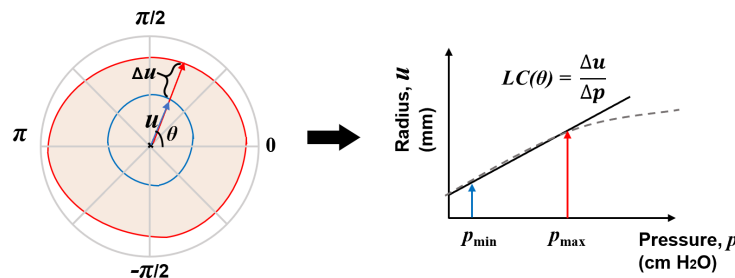

Fig. 1. Diagram presenting the definition of *LC*. Left: figure in polar coordinates with blue lines showing the geometry of the sample and its radius at *θ* when pressure is at its minimum, and red lines when pressure is at its maximum (displacement is exaggerated for clarity). Right: pressure versus displacement curve, in which *LC* is computed as the displacement with respect to change in pressure.

In order to determine the radii in the equation above, an appropriate choice of the origin is very important. In general, there are no landmarks in tracheas or in homogeneous samples, which provides no absolute coordinate system for reference. Unpredictable motion of the catheter and airway in aOCT scans leads to displacement of the airway surface from the catheter tip, even when there is no expansion or contraction of the airway. In order to robustly estimate the radial displacement, several possibilities for the definition of the origin were explored: 1) the catheter tip (which is how aOCT data is natively referenced), 2) the geometric centroid of the lumen at minimum pressure of the respiratory cycle, and 3) the geometric centroid of the lumen in each frame, (where a frame is an image of the lumen from one complete rotation of the aOCT probe), *i.e.*, a dynamic centroid. To assess the relative merits of each method, representative heat maps of the radial strain versus scan angle and time were computed from data of an inhomogeneous phantom under respiratory ventilation.

In the third and fourth respiratory cycles, slight and heavy motion was introduced to the phantom, respectively, to produce a sudden shift (Fig. 2).
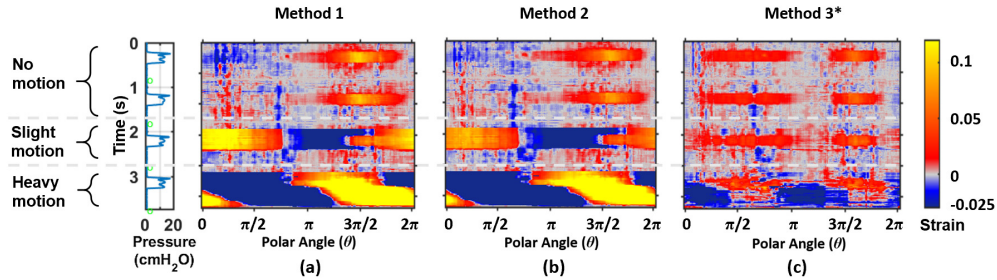

Fig. 2. Radial strain maps rendered with different methods for choosing the coordinate origin (Methods 1-3), produced from a scan of phantom B performed while motion was intentionally introduced. The notch of the phantom is located at $\theta = 3\pi/2$. In the first two respiratory cycles, no motion was introduced; in the third cycle, slight motion was introduced; in the fourth cycle, heavy motion was introduced. (a) Results produced by method 1: using catheter position as the origin. (b) Results produced by method 2: using the centroid of the frame at minimum pressure as the origin; (c) Results produced by method 3 (* the method in this paper): using the dynamic centroid as the origin.

In methods 1 and 2, in the absence of motion, the results demonstrate a repeated pattern of strain as a function of angle during each respiratory cycle. However, with even slight motion, large artifacts are induced which lead to irregular patterns of strain between successive respiratory cycles. In comparison, method 3 provides robust results with or without motion. In translation to clinical practice, we anticipate significant cardiac and respiratory motion. Hence, we chose the dynamic centroid method to eliminate motion artifacts and guarantee measurement stability.

With the method for choosing the coordinate origin established, *LC* was computed from lumen images and pressure data sampled simultaneously in time (*t*) as follows. At each time point, the centroid of the lumen was computed, and the radial distance and angle of the lumen contour relative to the centroid ($u_{\theta,t}$ and θ, respectively) were computed. The radial distance relative to the centroid, $u_{\theta,t}$, was then interpolated at evenly distributed values of θ with $\Delta\theta = 1°$. Subsequently, based on the respiratory rate, pressure in each respiratory cycle was analyzed, and the maximum and minimum pressures ($p_{\max}$ and $p_{\min}$, respectively) were determined, as well as their corresponding time points ($t_{\max}$ and $t_{\min}$). Then, for each respiratory cycle, the corresponding radial displacements were computed from $u_{\theta,t\max} - u_{\theta,t\min}$, and finally *LC* was computed according to Eq. (1). For each set of scans there were ≥ 3 respiratory cycles, and the reported *LC* was the average and standard deviation from all cycles. For radial strain maps, strain was computed at each θ and t according to $(u_{\theta,t} - u_{\theta,t\min}) / u_{\theta,t\min}$.

2.2 Preparation of samples

2.2.1 Elastic phantoms

Two phantoms of controlled elastic properties were designed and fabricated (as shown in Fig. 3) to mimic the compliance of real tracheas. The first phantom (phantom A) was used to validate the local compliance measurement of a simple tube of constant wall thickness and homogeneous elastic modulus (resulting in a constant *LC* around its circumference). The

second phantom (phantom B) was used to validate local compliance in a tube of known stiffness, but with non-uniform thickness, to provide non-uniform *LC*. The thickness was varied in the form of a notch over a small region of the circumference to locally increase *LC*, which loosely approximates the effect on *LC* of the open-ring structure of cartilage in the pig tracheas in this study. The notch of the phantom can be thought to represent the portion of the trachea corresponding to the trachealis muscle, which may be expected to produce an *LC* pattern that recapitulates that of airways. However, it is important to note that due to mechanical coupling over the circumference of the airway wall, *LC* may exhibit a spatial pattern that is non-local to the underlying tissue compliance, as will be shown in finite element modeling (FEM)-based simulations of the notched tube below.

Based on previous data from an OCT study of the change in the size of airways versus change in transpulmonary pressure [25], the circumferentially-averaged *LC* of the adult human trachea is estimated to be ~0.05 mm/cm H_2O. Our previous experiments [18] indicate that the averaged *LC* of pig tracheas ranges from ~0.0093 - 0.0233 mm/cm H_2O. Thus, we chose the elastomer polydimethylsiloxane (PDMS, 50 cSt viscosity, ClearCo, Inc.) as the raw material to prepare tube phantoms with appropriate radial thickness to match this range of *LC*. Dimensions of the two phantoms are listed in Table 1. Phantom A had a constant thickness of 1.43 mm. Phantom B had a thickness of 1.44 mm, except for a ~35° sector (B2) that has a thickness of 0.70 mm. Both phantoms had a constant inner radius of ~7.1 mm. The concentration ratio of PDMS curing agent (General Electric RTV-615 B and A, respectively, Circuit Specialists, Inc.) RTV-615 B: PDMS RTV-615 A: pure PDMS fluid is 1:10:10. Al_2O_3 powder (Sigma-Aldrich, #265497, 10 μm) was added with a concentration of 22 mg/g to produce sufficient light scattering for OCT. The same material was used to prepare a solid cylinder with an outer radius of 24.57 mm and height of 11.58 mm for measurement of Young's modulus (E_T). The Young's modulus was measured under quasi-static parallel plate compression with a commercial texture analyzer (TA.XT Plus, Texture Technologies, Scarsdale, NY).
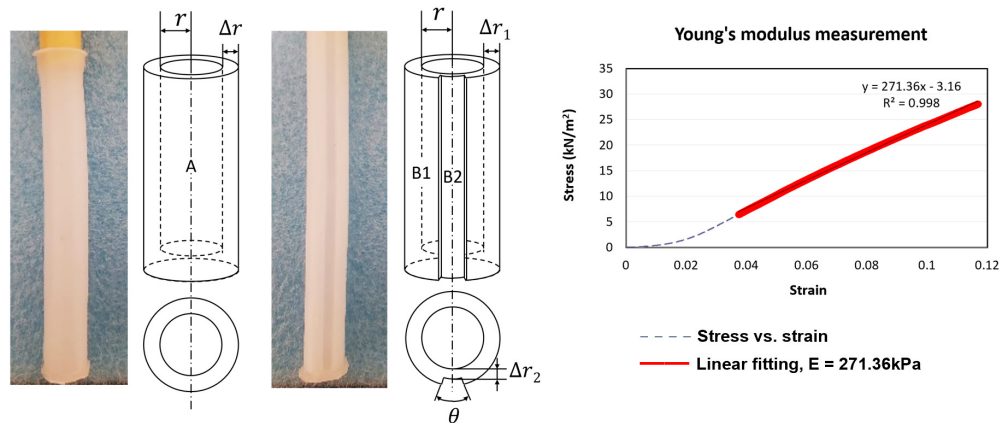

Fig. 3. Design of two phantoms with pictures and engineering diagrams. Phantom A (left) and Phantom B (middle) were made of PDMS, whose Young's modulus was measured by the texture analyzer. A representative plot showing the stress-strain relationship of the PDMS phantom material as obtained from the texture analyzer is presented on the right. The dotted line is the stress vs. strain curve, while the red line is the linear fitting curve whose slope is the Young's modulus.

Table 1. Properties of Phantoms*

Phantom	Inner Radius (r, mm)	Thickness (Δr, mm)	Angular extent (θ, degree)	Young's modulus (E_T, kPa)	LC (predicted) mm/cm H_2O
A	7.09 ± 0.14	1.43 ± 0.03	0 - 360	275 ± 6	0.0124 ± 0.0005
B1	7.08 ± 0.09	1.44 ± 0.02	0 - 325.4	275 ± 6	See Fig. 7 for Results
B2		0.70 ± 0.01	325.4 - 360		

* All data are presented as mean ± standard deviation.

The stress-strain behavior of the PDMS material measured by the texture analyzer (Fig. 3) exhibits high linearity up to a strain greater than that induced in the aOCT experiments. As such, we treat the PDMS as a linear, isotropic material and employ a thick-walled tube model to compute the theoretical local compliance of phantom A. Based on the model described in our previous work [18], LC is derived based on the relationship between displacement and pressure:

$$LC = \frac{\Delta u}{\Delta p} = rx \tag{2}$$

$$\text{where } x = \frac{1}{E} \frac{(r+\Delta r)^2 (1+v) + r^2 (1-2v)}{\left((r+\Delta r)^2 - r^2\right)} \tag{3}$$

In these formulas, Δu and Δp are the displacement and change in pressure, r is the inner radius of the tube, Δr is the thickness of the tube, E is the Young's modulus of the material, and v is the Poisson's ratio of the material, the latter of which is taken to be 0.495 [29]. Finally, based on the measured Young's modulus, Poisson's ratio and the dimensions described above, the predicted LC of phantom A is 0.0124 ± 0.0005 mm/cm H_2O.

For phantom B, the thick-walled tube model is no longer applicable due to the variable wall thickness. Therefore, the local compliance was estimated by using a finite element model (FEM) implemented with the FreeFEM software (Code 1, Ref. [30]), which was used to simulate the deformation of the phantom under different pressures. For an isotropic material, with the known dimensions provided in Table 1, measured Young's modulus and assumed Poisson's ratio of 0.495, the FEM of phantom B was built to predict deformation. The output of FreeFEM was exported and the coordinates of each point on the interior surface of the phantom before and after deformation were used to calculate LC. The results are discussed below.

2.2.2 Ex vivo tracheas

Six trachea specimens were dissected from domestic pigs weighing 50 to 60 pounds and frozen. Each specimen included the complete larynx, trachea, pig bronchus, lung and heart. All experimental procedures were approved by the Institutional Animal Care and Use Committee at North Carolina State University (IACUC No.16-187). Samples were thawed and allowed to equilibrate to room temperature before experiments. Three of the six specimens were sutured along the length of the tracheas at the opening of the cartilage (posterior airway) with metallic threads to act as fiducial markers. The pig bronchus and main bronchi were sutured to prevent air leakage from lungs. Cuffed endotracheal tubes (ETT) were inserted to tracheas and inflated to form a seal. A double swivel adapter with plastic diaphragm was used to connect the ETT for ventilation. The diaphragm was drilled to allow the aOCT and pressure catheters to pass through without causing air leakage. After aOCT scans, tracheas were dissected into small ring sections, and fixed in 10% formalin. Then, the formalin-fixed, paraffin-embedded (FFPE) samples were sectioned into 4-micron slices and subsequently stained with hematoxylin and eosin (H&E).

2.3 System hardware

To acquire real-time data for this study, a system comprised of a ventilator and an endoscopic aOCT system with integrated pressure sensing catheter was used, which has been described in detail previously [26]. Briefly, the aOCT system uses light from a swept-source laser (SL1310V1, Thorlabs Inc) through a Mach-Zehnder interferometer to produce OCT signals, as shown in Fig. 4(a). The fiber-optic catheter (170 cm long, ~0.85 mm in diameter) transmits light into the lumen and provides rotational scans under the control of a rotation / translation scanner (Fig. 4(b)-(c)). The measured axial resolution of the system is 12.6 µm and the signal-to-noise ratio (SNR) is 105.7 dB at 1.8 mm. The ventilator controls the pressure with the desired rate and amplitude. An intraluminal pressure sensor (SPR-330A, Millar Inc.) with a sensitivity of ~1.32 cm H_2O is utilized to measure the *in situ* pressure inside the airway, as this pressure has been found to be significantly different from that measured at the ventilator [26], which is crucial for quantitative elastography.
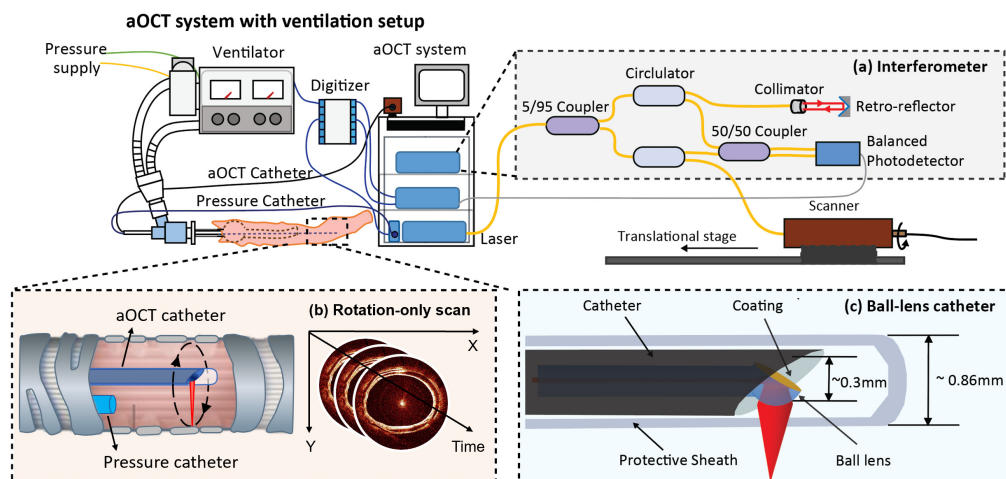

Fig. 4. Diagram of aOCT system setup with the ventilator and the pressure catheter. (a) Mach-Zehnder interferometer from the aOCT system; (b) aOCT and pressure catheters inside the airway and scan pattern with rotation only (no pullback); the pressure catheter is several centimeters away from the OCT catheter to avoid blocking its view; produced aOCT images are time-resolved. (c) The ball-lens structure at the tip of the aOCT catheter: the outer diameter of the catheter including the sheath is around 0.86 mm, suitable for airway elastography with minimal impact on pressure measurement.

2.4 Imaging protocol

aOCT scans were collected at an A-line rate of 100 kHz during rotation at 20 Hz (no pullback) to capture repeated images of one cross-section of the airway lumen over ≥3 respiratory cycles. The ventilator was set to run in pressure-controlled ventilation (PCV) mode with a respiratory rate of 20 breaths/min. The maximum inspiratory pressure (MIP) was set to a value between 10 and 18 cm H_2O to avoid excessively high tidal volumes. At the beginning of each experiment, the aOCT and intraluminal pressure catheters were inserted via the ETT into the prepared phantoms or tracheas. The aOCT catheter was approximately centered within the lumen to minimize distortion or imaging artifacts. Then, aOCT scans were performed with the pressure value simultaneously digitized at 5 kHz. The air-tissue interface from each aOCT image was later segmented using a semi-automatic segmentation method described elsewhere [31]. The segmentations provided coordinates of each point on the airway wall surface, which was used to calculate displacement as described above. With known displacement and pressure data, the measured compliance was calculated and averaged as described in 2.1 to obtain one value of *LC* for each polar angle.

3. Results

3.1 Phantom scans

3.1.1 Phantom with uniform thickness (A)

A representative aOCT image and corresponding LC measurements of phantom A are presented in Fig. 5. In the OCT image, both inner and outer surfaces of the phantom are clearly identified. Phantom deformation under dynamic pressure is captured, as shown in Fig. 5(c). According to the thick-walled tube model, the phantom is predicted to have a constant LC of 0.0124 ± 0.0005 mm/cm H_2O over the entire circumferential range of 2π. The aOCT-measured LC is 0.0135 ± 0.0010 mm/cm H_2O over the circumference of the airway. The difference between the mean measured and predicted values is 0.0012 mm/cm H_2O, or ~9% of the predicted value, and lies within experimental error. The angle-resolved LC is plotted in Fig. 5(b). Variations in LC as a function of angle might arise from the inaccurate measurement of phantom geometry caused by the sagging of OCT catheter. Non-uniform rotation distortion (NURD), which is a general problem for most proximally-scanned endoscopic catheters [32], could also lead to error in measurement. Pressure sensing fluctuation of up to $\pm$ 2 cm H_2O also contributes to the error. However, overall, the variation of LC over θ tends to be relatively stable, varying by approximate $\pm$ 7.5% of the mean value.
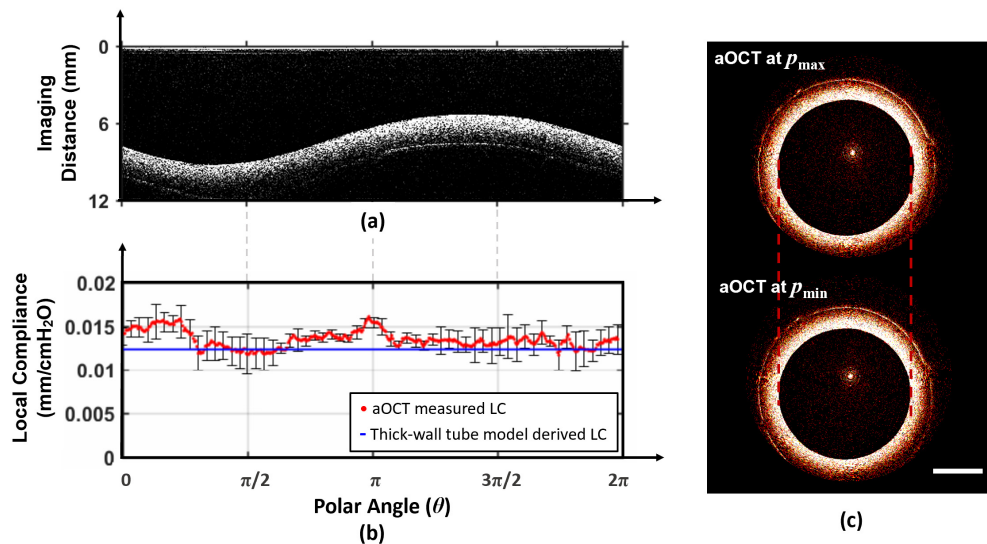

Fig. 5. aOCT scan and corresponding LC measurement of phantom A. (a) The OCT image in polar coordinates with an x-coordinate of θ ranging from 0 to 2π, and a y-coordinate of imaging distance away from the OCT catheter ranging from 0 to 12 mm; (b) Circumferentially-resolved LC with the blue line representing predicted LC and red dots representing measured LC; error bars represent the standard deviation of LC over multiple respiratory cycles; (c) The OCT image in Cartesian coordinates showing phantom deformation under different pressures. Scale bar: 5 mm

3.1.2 Phantom with notch (B)

The FEM simulation of phantom B is shown in Fig. 6. To visualize phantom deformation under different pressure levels, inner surfaces under minimum and maximum pressure are plotted with their centroids overlaid (Fig. 6(c)). In the plots, the center of notch is located along the negative y-axis ($3\pi/2$ in polar coordinates). According to the FEM results, larger radial deformation is observed along the y-axis, while very little deformation observed in the x direction. The largest deformation appears where the notch is located along the $-y$ axis, where the increased compliance directly correlates to the decreased wall thickness.

Importantly, there is a second peak in deformation located along the $+ y$ axis, exactly 180 degrees (opposite) the location of the notch. This can be understood as a folding effect due to the mechanical coupling across the circumference of the tube when under radial stress. In the limit of very high deformation for a tube with a very small notch, one would observe lumen deformation into the shape of a teardrop, where the centroid of the teardrop would be positioned such that positive deformation is observed on both ends of the drop (both the pointed end, where the notch exists, and the opposite end).

aOCT experiments corresponding to the modeled data are summarized in Fig. 7. aOCT-measured LC is in good agreement with the predicted results (Fig. 7(b)), with the largest LC occurring at $\theta = 3\pi/2$, where the notch is located, as well as a second peak in LC located at $\theta = \pi/2$. Compared to phantom A, obvious heterogeneity in LC is observed with phantom B. The average error between the measured and predicted LC is 0.0049 ± 0.0034 mm/cm H_2O. Notably, the error is not normally distributed, as can be seen in Fig. 7(d) and e. Larger error is observed near $\theta = 3\pi/2$, which may be attributed to imperfections in notch fabrication. Another possible reason is NURD, which is θ dependent. A very small degree of rotation is also observed with phantom B within each respiratory cycle (see video in Visualization 1), which could be caused by catheter vibration under dynamic pressure and was not accounted for in our analysis.
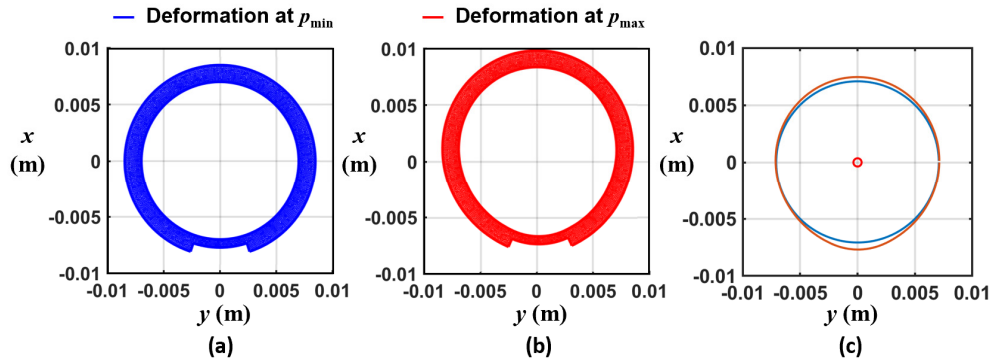

Fig. 6. FEM simulation of phantom B. (a) Phantom with no overpressure; (b) Phantom at maximum luminal overpressure of 18 cm H_2O; (c) Comparison of the inner surface of the phantom under different luminal pressures with their centroid overlaid.
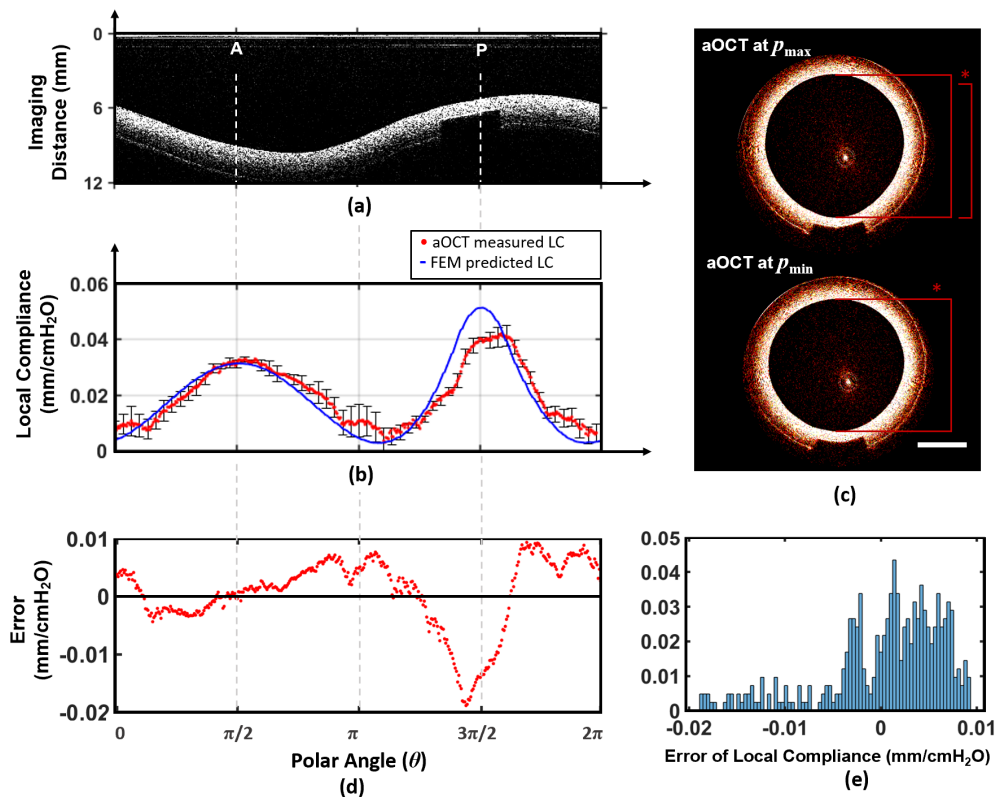
Fig. 7. Phantom B scan results. (a) Raw OCT image with the notch centered at $3\pi/2$. (b) Corresponding LC measurement with blue line indicating the predicted LC from FEM simulation, and red dot indicating aOCT-measured LC with error bars represent the standard deviation of LC over different respiratory cycles. (c) aOCT images of the notched tube in Cartesian coordinates with comparison of the diameter in y-axis under maximum and minimum pressure (marked as *). (d) Error in LC (aOCT − FEM) as a function of θ, and (e) corresponding histogram of error showing the distribution of the error values. Scale bar: 5 mm.

3.2 Ex vivo trachea scans

Scans of *ex vivo* porcine tracheas were performed to further assess the ability of aOCT to measure LC in animal specimens. To understand the effects of the underlying tissues on the observed LC, histological analysis of the tracheas was subsequently performed. Representative histological and aOCT images are shown in Fig. 8. In both images, structures such as the epithelium, cartilage and trachealis muscle are easily identified. Among these structures, cartilage and the trachealis muscle are expected to contribute the most to the biomechanical properties of the airway. In the porcine trachea, cartilage, which exhibits hypo-scattering (is dark) in aOCT images, appeared as a C-shaped ring, and the trachealis muscle bridges the gap at the cartilage opening in the posterior airway. In some cases, a structure that appears like the cartilage opening is observed, but upon further inspection is identified as the interface of two cartilage pieces. To differentiate the real opening from these cartilage interfaces, scans from adjacent cross-sections were used to assess whether the apparent opening persists along the length of the airway.
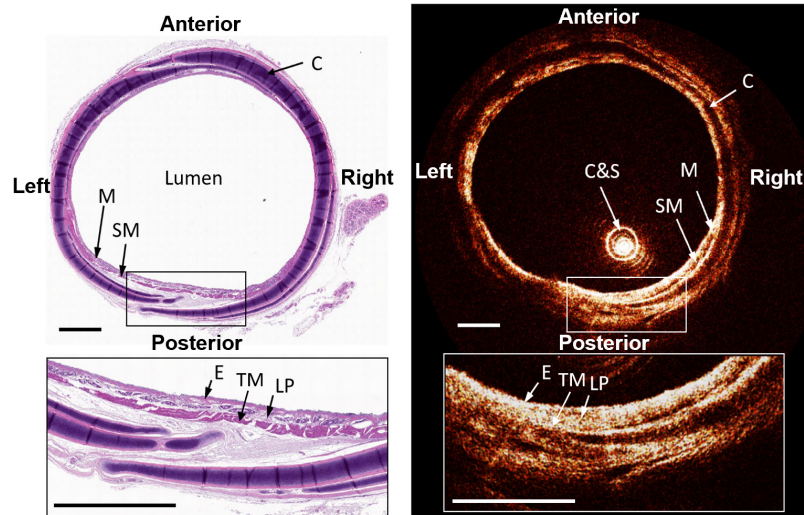
Fig. 8. Histological and aOCT images of *ex vivo* porcine trachea. Left: representative histological image (H&E); Right: representative aOCT scan of the same trachea. The zoomed-in regions display the cartilage opening at the posterior airway. M, mucosa; SM, submucosa; C, cartilage; E, epithelium; LP, lamina propria; TM, trachealis muscle; C&S, aOCT catheter and sheath; Scale bar: 2 mm.

Representative aOCT results of two *ex vivo* tracheas are shown in Fig. 9. Among the 6 tracheas, three of them had fiducial markers. The fiducial markers were placed in the posterior airway, where the trachealis muscle is located. In the plots, the posterior airway is located at $\theta = 3\pi/2$. Typical results from one of these tracheas with fiducial markers is shown in Fig. 9(a)-(c). In the computed *LC* curve, there are peaks at the anterior and posterior tracheal wall. The highest *LC* occurs at the posterior where the cartilage opens (Fig. 9(b)). Identical conclusions are obtained in tracheas without fiducial markers, with one representative scan shown in Fig. 9(d)-(f). In this trachea, higher *LC* is also observed at the anterior and the posterior direction, and the largest *LC* at the posterior (Fig. 9(e)), consistent with where the cartilage opening was identified by examining the subsurface structure (Fig. 9(d)-(f)).
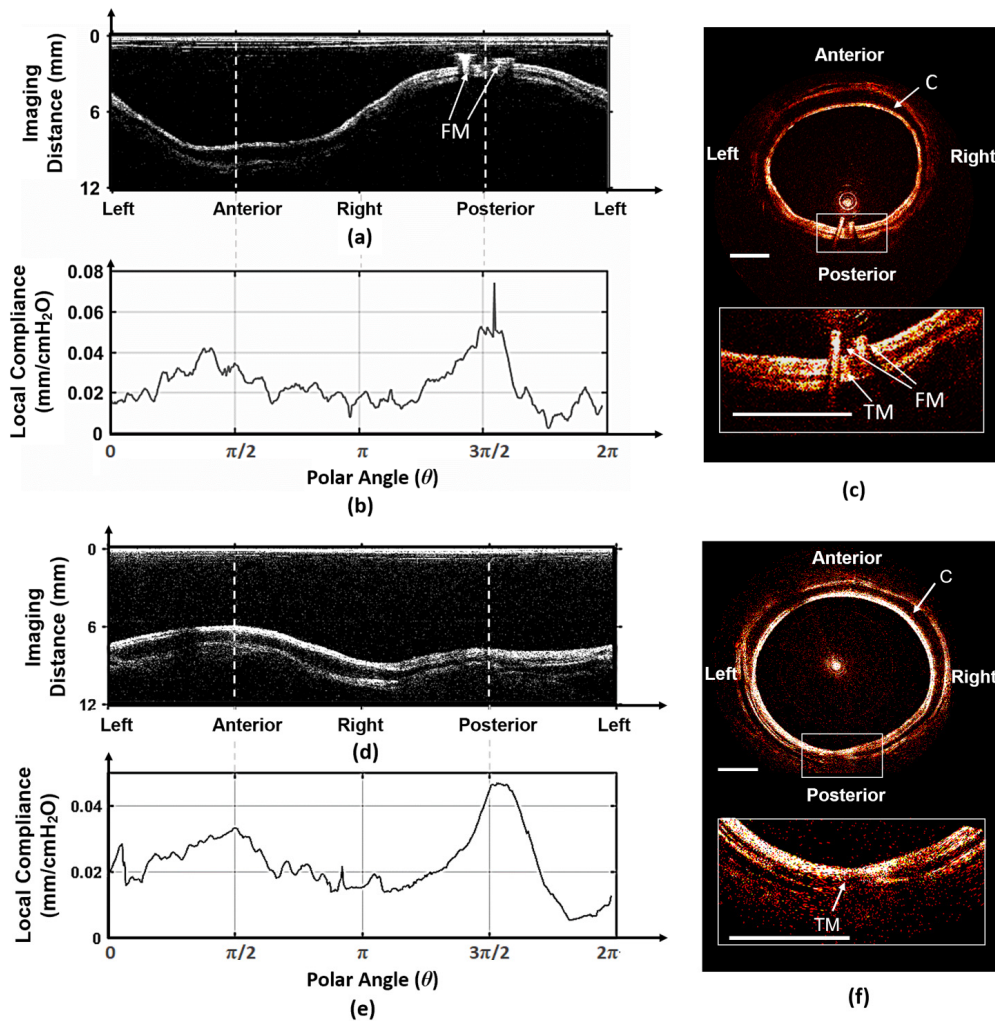
Fig. 9. *Ex vivo* scan results of pig trachea. (a-c) Trachea with fiducial markers at the cartilage opening. (d-f) Trachea without any fiducial marker. In both scans, the OCT image in polar coordinates (a, d) has an *x*-coordinate of angle ranging from 0 to 2π, and a *y*-coordinate of imaging distance away from the OCT catheter ranging from 0 to 12 mm. Positions of left, anterior, right and posterior airway is marked on the *x*-axis. Circumferentially-resolved *LC* is plotted in (b, e). The OCT images in Cartesian coordinates (c, f) show the endoscopic view of tracheas with the zoomed-in window indicating the location of trachealis muscle. C, cartilage; TM, trachealis muscle; FM, fiducial marker; Scale bar: 5 mm.

For all *ex vivo* tracheas ($N = 6$), box-and-whisker plots were made for *LC* measurements centered at the left, anterior, right and posterior wall, as shown in Fig. 10. For each trachea, 30 samples ranging over 0.17π are included at each position. The findings from these six *LC* scans are generally consistent, with highest compliance at the posterior corresponding to the cartilage ring opening, second highest compliance located opposite to the opening in the anterior, and relatively lower compliances measured to the right and left.
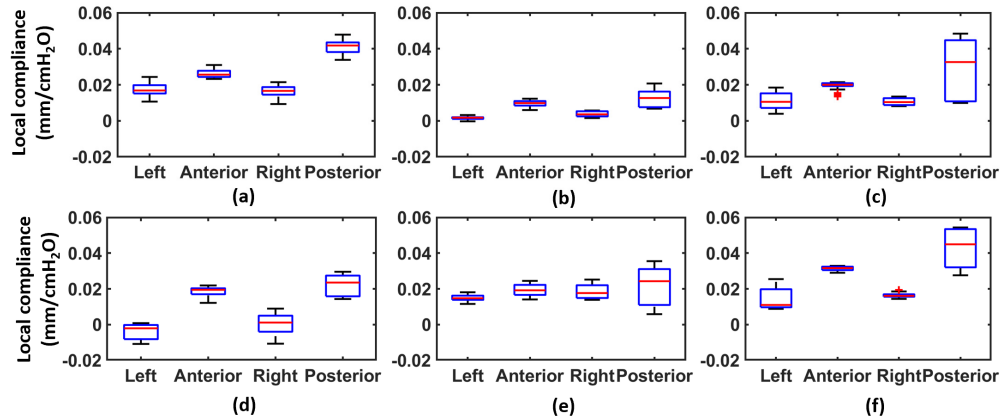
Fig. 10. Box-whisker plots of *LC* measured in six *ex vivo* pig tracheas. (a-c) Tracheas with fiducial markers; (d-f) Tracheas without fiducial marker. In all figures, along *x*-axis are the positions at where *LC* was analyzed, including left, anterior, right and posterior airway; *y*-axis is the measured *LC*.

4. Discussion

To the best of our knowledge, this is the first demonstration of aOCT elastography validated in a mechanically heterogeneous phantom via computational (finite element) modelling, as well as the first time such modeling was used to predict features of real airway tissue compliance. To achieve this outcome, we developed a robust aOCT elastography method that quantifies *LC* to indicate differences in tissue stiffness and/or thickness in the circumferential direction. An elastic tube-shaped phantom with uniform thickness was fabricated, and an analytical model was used to validate the magnitude of *LC* extracted by aOCT, which was within 9%. Then, a heterogeneous phantom was fabricated with a notch along its length, and FEM employed to validate the pattern of *LC* measured by aOCT. aOCT-derived compliance data exhibited both the correct pattern and magnitude of *LC* in comparison to the model, with a primary peak in *LC* corresponding to the location of the notch, and a second, weaker peak in *LC* at a position directly opposite to the notch. Finally, *ex vivo* trachea elastography was demonstrated, which provided measurements that were robust and consistent in the pattern of *LC* (left, anterior, right, posterior) across *N* = 6 tracheas. Furthermore, the magnitude of *LC* obtained from tracheas was consistent with that estimated from previous findings in pigs, rabbits and humans [17,18,25].

Porcine tracheas are comprised of a relatively stiff cartilage open ring structure embedded within softer smooth muscle. To the extent that the cartilage ring opening provides a similar pattern of compliance to the notched tube phantom (B), the findings from the *ex vivo* scans can be compared to those from the phantom. It is intuitive to understand that the highest *LC* occurs in regions of tissue (or tube material) where the elasticity is lower (or wall thickness is lower) than the surrounding wall. The location of the *LC* peak in tracheas is consistent with the histologic data, in which the C-shaped cartilage is bridged with trachealis muscle at the posterior wall. However, the second peak of *LC* that appears opposite the wall inhomogeneity is less intuitive and can be thought of as a folding effect. Importantly, this second, slightly lower peak in *LC* is predicted by the FEM model in the notched phantom and observed both in aOCT scans of the phantom and the tracheas at a position opposite the primary peak. This highlights that, while it may be possible to identify a single elastic inhomogeneity by merit of the largest change in *LC*, interpretation of *LC* results should be guided by anatomical considerations and FEM modeling when possible. In this case, the second, weaker peak in *LC* does not correspond to a second elastic inhomogeneity but is instead an artifact of the first. These findings suggest that aOCT can be used to assess *LC* in heterogeneous tissues and

could potentially be applied to detect abnormalities and aid in diagnosis and treatment of airway diseases.

Other groups have also studied the compliance in airways for the local stiffness in circumferential direction. For example, "wall compliance" defined as the inverse of the tangential modulus of the tissue and the wall thickness is used to assess central airway elasticity [17]. "Specific compliance" derived from MRI imaging of upper airway as the change of normalized displacement over different constant pressures can evaluate the stiffness of upper airways [8]. Both methods are effective but have not been linked to the physical structure of airways, such as varying thickness of the airway wall. In our method, the increase in local compliance is consistent with the location of the abnormality (cartilage ring opening) as well as a second, weaker peak in the mirrored (opposite) position, suggesting that with appropriate understanding of airway wall anatomy and mechanical model-based interpretation of results, the method can provide assessment of heterogeneous wall properties.

This method offers several advantages relevant to future clinical translation for upper and central airway elastography. First, imaging using aOCT is readily coupled with routine bronchoscopy [33], the light itself is non-invasive, and rapid scans minimize patient discomfort. An intraluminal pressure catheter can be readily coupled with the aOCT catheter for *in vivo* assessment of pressure-volume [26], enabling quantitative compliance measurement [18]. Finally, aOCT scans can be further performed with pullback (as in [18]) on subjects under respiration to collect data over the length of the airway; this will require further development of sampling protocols to collect $(3 + 1)$D airway images by aOCT. However, systematic error caused by catheter vibration or NURD has always been a problem in OCT endoscopy, and continued efforts such as correction based on speckle decorrelation [34] or the usage of a torque coil in the OCT catheter [35] are needed to mitigate error before reliable in-human imaging can be viable.

In conclusion, aOCT-based elastography provides an accurate and robust measurement of local airway wall compliance. In combination with FEM simulations, aOCT elastograms provide insight into the underlying tissue mechanical properties. This method has the ready potential to be adopted to a routine airway endoscopy for the diagnosis and treatment of airway obstructive disorders and the study of dynamic airway collapse.

Disclosures

The authors declare that there are no conflicts of interest related to this article.

References

1. Y. K. Mariappan, K. J. Glaser, and R. L. Ehman, "Magnetic resonance elastography: a review," Clin. Anat. **23**(5), 497–511 (2010).
2. L. E. Bilston and S. C. Gandevia, "Biomechanical properties of the human upper airway and their effect on its behavior during breathing and in obstructive sleep apnea," J. Appl. Physiol. **116**(3), 314–324 (2014).
3. J. Cisonni, A. D. Lucey, J. H. Walsh, A. J. C. King, N. S. J. Elliott, D. D. Sampson, P. R. Eastwood, and D. R. Hillman, "Effect of the velopharynx on intraluminal pressures in reconstructed pharynges derived from

individuals with and without sleep apnea," J. Biomech. **46**(14), 2504–2512 (2013).

4. M. Eskandari, A. L. Arvayo, and M. E. Levenston, "Mechanical properties of the airway tree: heterogeneous and anisotropic pseudoelastic and viscoelastic tissue responses," J. Appl. Physiol. **125**(3), 878–888 (2018).

5. K. A. Carden, P. M. Boiselle, D. A. Waltz, and A. Ernst, "Tracheomalacia and tracheobronchomalacia in children and adults: an in-depth review," Chest **127**(3), 984–1005 (2005).

6. L. Javia, M. A. Harris, and S. Fuller, "Rings, slings, and other tracheal disorders in the neonate," Semin. Fetal Neonatal Med. **21**(4), 277–284 (2016).

7. U. Holzhäuser and R. K. Lambert, "Analysis of tracheal mechanics and applications," J. Appl. Physiol. **91**(1), 290–297 (2001).

8. D. R. Subramaniam, G. Mylavarapu, K. McConnell, R. J. Fleck, S. R. Shott, R. S. Amin, and E. J. Gutmark, "Compliance Measurements of the Upper Airway in Pediatric Down Syndrome Sleep Apnea Patients," Ann. Biomed. Eng. **44**(4), 873–885 (2016).

9. B. C. Goss, K. P. McGee, E. C. Ehman, A. Manduca, and R. L. Ehman, "Magnetic resonance elastography of the lung: technical feasibility," Magn. Reson. Med. **56**(5), 1060–1066 (2006).

10. M. Yin, J. A. Talwalkar, K. J. Glaser, A. Manduca, R. C. Grimm, P. J. Rossman, J. L. Fidler, and R. L. Ehman, "Assessment of hepatic fibrosis with magnetic resonance elastography," Clin. Gastroenterol. Hepatol. **5**(10), 1207–1213 (2007).

11. J.-H. Jiang, J. F. Turner, Jr., and J.-A. Huang, "Endobronchial ultrasound elastography: a new method in endobronchial ultrasound-guided transbronchial needle aspiration," J. Thorac. Dis. **7**(Suppl 4), S272–S278 (2015).

12. A. Rozman, M. M. Malovrh, K. Adamic, T. Subic, V. Kovac, and M. Flezar, "Endobronchial ultrasound elastography strain ratio for mediastinal lymph node diagnosis," Radiol. Oncol. **49**(4), 334–340 (2015).

13. R. G. Michel, G. T. Kinasewitz, K.-M. Fung, and J. I. Keddissi, "Optical coherence tomography as an adjunct to flexible bronchoscopy in the diagnosis of lung cancer: a pilot study," Chest **138**(4), 984–988 (2010).

14. J. Schmitt, "OCT elastography: imaging microscopic deformation and strain of tissue," Opt. Express **3**(6), 199–211 (1998).

15. X. Liang, A. L. Oldenburg, V. Crecea, E. J. Chaney, and S. A. Boppart, "Optical micro-scale mapping of dynamic biomechanical tissue properties," Opt. Express **16**(15), 11052–11065 (2008).

16. K. M. Kennedy, L. Chin, R. A. McLaughlin, B. Latham, C. M. Saunders, D. D. Sampson, and B. F. Kennedy, "Quantitative micro-elastography: imaging of tissue elasticity using compression optical coherence elastography," Sci. Rep. **5**(1), 15538 (2015).

17. C. Robertson, S.-W. Lee, Y.-C. Ahn, S. Mahon, Z. Chen, M. Brenner, and S. C. George, "Investigating in vivo airway wall mechanics during tidal breathing with optical coherence tomography," J. Biomed. Opt. **16**(10), 106011 (2011).

18. R. Bu, S. Balakrishnan, N. Iftimia, H. Price, C. Zdanski, and A. L. Oldenburg, "Airway compliance measured by anatomic optical coherence tomography," Biomed. Opt. Express **8**(4), 2195–2209 (2017).

19. J. J. Armstrong, M. S. Leigh, D. D. Sampson, J. H. Walsh, D. R. Hillman, and P. R. Eastwood, "Quantitative upper airway imaging with anatomic optical coherence tomography," Am. J. Respir. Crit. Care Med. **173**(2), 226–233 (2006).

20. B. J. F. Wong, R. P. Jackson, S. Guo, J. M. Ridgway, U. Mahmood, J. Su, T. Y. Shibuya, R. L. Crumley, M. Gu, W. B. Armstrong, and Z. Chen, "In vivo optical coherence tomography of the human larynx: normative and benign pathology in 82 patients," Laryngoscope **115**(11), 1904–1911 (2005).

21. O. Ajose-Popoola, E. Su, A. Hamamoto, A. Wang, J.-C. Jing, T. D. Nguyen, J. J. Chen, K. E. Osann, Z. Chen, G. S. Ahuja, and B. J. F. Wong, "Diagnosis of subglottic stenosis in a rabbit model using long-range optical coherence tomography," Laryngoscope **127**(1), 64–69 (2017).

22. S.-W. Lee, A. E. Heidary, D. Yoon, D. Mukai, T. Ramalingam, S. Mahon, J. Yin, J. Jing, G. Liu, Z. Chen, and M. Brenner, "Quantification of airway thickness changes in smoke-inhalation injury using in-vivo 3-D endoscopic frequency-domain optical coherence tomography," Biomed. Opt. Express **2**(2), 243–254 (2011).

23. M. Kirby, K. Ohtani, R. M. Lopez Lisbona, A. M. D. Lee, W. Zhang, P. Lane, N. Varfolomeva, L. Hui, D. Ionescu, H. O. Coxson, C. MacAulay, J. M. FitzGerald, and S. Lam, "Bronchial thermoplasty in asthma: 2-year follow-up using optical coherence tomography," Eur. Respir. J. **46**(3), 859–862 (2015).

24. C. Sun, B. Standish, and V. X. D. Yang, "Optical coherence elastography: current status and future applications," J. Biomed. Opt. **16**(4), 043001 (2011).

25. J. P. Williamson, R. A. McLaughlin, W. J. Noffsinger, A. L. James, V. A. Baker, A. Curatolo, J. J. Armstrong, A. Regli, K. L. Shepherd, G. B. Marks, D. D. Sampson, D. R. Hillman, and P. R. Eastwood, "Elastic properties of the central airways in obstructive lung diseases measured using anatomical optical coherence tomography," Am. J. Respir. Crit. Care Med. **183**(5), 612–619 (2011).

26. S. Balakrishnan, R. Bu, N. Iftimia, H. Price, C. Zdanski, and A. L. Oldenburg, "Combined anatomical optical coherence tomography and intraluminal pressure reveal viscoelasticity of the in vivo airway," J. Biomed. Opt. **23**(10), 1–4 (2018).

27. P. Tozzi, D. Hayoz, A. F. Corno, I. Mallabiabarrena, and L. K. von Segesser, "Cross-sectional compliance overestimates arterial compliance because it neglects the axial strain," Swiss Med. Wkly. **133**(33-34), 461–464 (2003).

28. S. R. Klein, L. Goldberg, R. M. Miranda, P. Bosco, R. J. Nelson, and R. A. White, "Effect of suture technique on arterial anastomotic compliance," Arch. Surg. **117**(1), 45–47 (1982).

29. A. Müller, M. C. Wapler, and U. Wallrabe, "A quick and accurate method to determine the Poisson's ratio and the coefficient of thermal expansion of PDMS," Soft Matter **15**(4), 779–784 (2019).

30. R. Bu, "FreeFEM code for phantom B," https://doi.org/10.6084/m9.figshare.8006717 (2019).

31. H. B. Price, J. S. Kimbell, R. Bu, and A. L. Oldenburg, "Geometric Validation of Continuous, Finely Sampled 3-D Reconstructions From aOCT and CT in Upper Airway Models," IEEE Trans. Med. Imaging **38**(4), 1005–1015 (2019).

32. Y. Kawase, Y. Suzuki, F. Ikeno, R. Yoneyama, K. Hoshino, H. Q. Ly, G. T. Lau, M. Hayase, A. C. Yeung, R. J. Hajjar, and I.-K. Jang, "Comparison of nonuniform rotational distortion between mechanical IVUS and OCT using a phantom model," Ultrasound Med. Biol. **33**(1), 67–73 (2007).

33. K. Wijesundara, C. Zdanski, J. Kimbell, H. Price, N. Iftimia, and A. L. Oldenburg, "Quantitative upper airway endoscopy with swept-source anatomical optical coherence tomography," Biomed. Opt. Express **5**(3), 788–799 (2014).

34. N. Uribe-Patarroyo and B. E. Bouma, "Rotational distortion correction in endoscopic optical coherence tomography based on speckle decorrelation," Opt. Lett. **40**(23), 5518–5521 (2015).

35. M. J. Gora, M. J. Suter, G. J. Tearney, and X. Li, "Endoscopic optical coherence tomography: technologies and clinical applications [Invited]," Biomed. Opt. Express **8**(5), 2405–2444 (2017).